CoaxHaptics-3RRR: A Novel Mechanically Overdetermined Haptic Interaction Device Based on a Spherical Parallel Mechanism

Huseyin Tugcan Dinc[1], Thomas Hulin[2,3], Michael Rothammer[5], HyeonSeok Seong[1], Bertram Willberg[2], Benedikt Pleintinger[2], Jee-Hwan Ryu[1], Christian Ott[2,4]

***Abstract*— This paper presents the CoaxHaptics-3RRR, a novel concept for haptic interaction devices that is based on a 3-RRR spherical parallel mechanism (SPM). The novelty lies in its mechanical overdetermination through a central hollow shaft, which brings two advantages. First, the device can be built with high rigidity with regard to translational degrees of freedom (DoF). Second, it enables a lighter design with less rotational inertia, as the moving links do not need to withstand translational or gravitational forces. In order to fully exploit these advantages, an optimization process has been conducted that simultaneously optimized for workspace, manipulability, inertia, and structural stiffness. The resulting functional demonstrator provides an unlimited workspace around the shaft axis and +/- 55 degrees in the other two rotational DoF, thus covering a large portion of the human wrist's rotational range. Tests confirm the validity and superiority of the concept over existing devices, making it a promising solution for the category of mechanically overdetermined haptic devices.**

I. Introduction

Ever since Raymond Goertz in Argonne National Lab invented a pure mechanically driven haptic interface for nuclear waste handling [1], numerous kinesthetic haptic devices have been developed to provide force feedback in various applications, such as minimally invasive surgery, space, and gaming. The PHANToM [2], the first commercial haptic device, boosted haptics research in many aspects. It has a serial kinematics with 6 degrees of freedom (DoF), of which the 3 translational ones were active, while the rotational movements were formed by a passive gimbal. Later, several parallel haptic devices were developed, such as the Omega.3 [3] and the Novint Falcon [4] with 3-DoF each, and the DeltHaptics [5] and the Octo [6] with active 6-DoF respectively.

Although several types and structures of haptic devices have been designed and commercialized, most of them can render translational force only, while rotational DoF are realized with passive mechanisms. Only a few devices provide active rotational DoF, such as the PHANToM Premium 1.5/6-DoF [7] and the Sigma.7 [8]. Those devices incorporate serial mechanisms at the end of the translational mechanism to achieve the rotational DoF. However, such actuated rotational serial mechanisms significantly increase moving inertia and mechanical compliance, compromising both translational and rotational feedback capabilities.

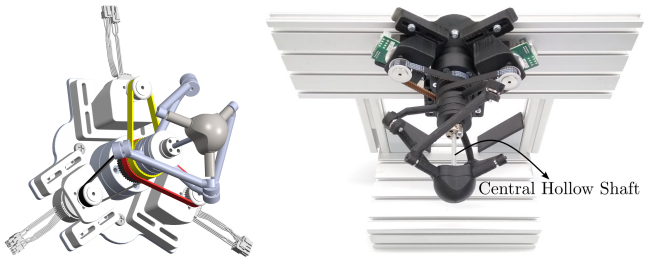

(a) CAD (front left view)

(b) real device (top front view)

Fig. 1: CAD model and photograph of the newly introduced CoaxHaptics-3RRR.

A natural progression in research involves developing a haptic device utilizing parallel-type rotational DoF. While serial mechanisms, like the PHANToM, often provide larger workspaces, parallel mechanisms such as the Omega.3, typically offer higher structural stiffness and lower dynamic inertia. Hybrid mechanisms aim to combine the advantages of both serial and parallel mechanisms [9], [10]. However, only limited research has explored parallel and hybrid mechanisms for rotational DoF due to the high design complexity. Examples for such devices are the *Sigma.7* [8], the mechanism of Millman and Colgate [9], and the device from Qin et al. [11].

On the other hand, so-called spherical parallel mechanisms (SPM) represent a technical possibility to take advantage of parallel mechanisms for rotational DoF, particularly for higher stiffness and lower dynamic inertia robotic end-effectors representing orientation [12]. Asada and Granito presented a robotic wrist joint with a coaxial input link based on an SPM [13]. Gosselin et al. introduced a new parallel solution for an SPM intended to serve as a camera orientation device for high-speed imaging [14].

Birglen et al. [15] first found the possibility of using SPM as a rotational haptic device and introduced SHaDe, the

[1]IRiS Lab., Korea Advanced Institute of Science and Technology (KAIST), 34141 Daejeon, South Korea. (e-mail : htdinc@kaist.ac.kr)

[2]Institute of Robotics and Mechatronics, German Aerospace Center (DLR), 82234 Wessling, Germany.

[3]Centre for Tactile Internet with Human-in-the-Loop (CeTI).

[4]TU Wien, Automation and Control Institute, 1040 Vienna, Austria.

[5]Hapticslabs GmbH, 01067 Dresden, Germany.

This work was funded by the German Research Foundation (DFG, Deutsche Forschungsgemeinschaft) as part of Germany's Excellence Strategy – EXC2050/1 – Project ID 390696704 – Cluster of Excellence "Centre for Tactile Internet with Human-in-the-Loop" (CeTI) of Technische Universität Dresden.

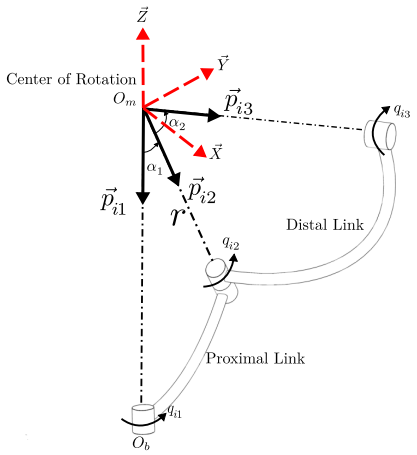

Fig. 2: A kinematic chain of a single leg of an SPM showing the kinematic relations.

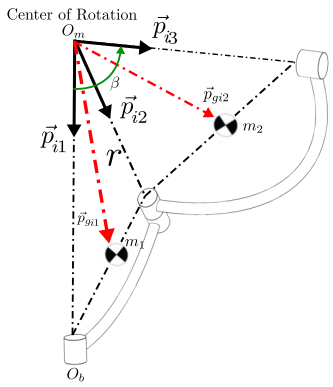

Fig. 3: Approximated center of mass locations of SPM.

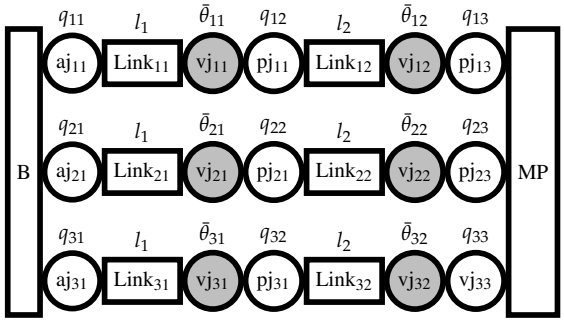

Fig. 4: Compliant kinematics model of the SPM and its virtual joint model where aj_{ik} is active joint, pj_{ik} is passive joint, vj_{ik} is virtual joint (with $i \in \{1,2,3\}$ and $k \in \{1,2\}$), MP is mobile platform, B is base, l_1 and l_2 are the lengths of proximal and distal links (adapted from [19]).

first rotational haptic device based on an SPM. They argued that SPMs have well-suited properties for haptic devices, specifically low inertia with an extremely low coupling among DoF, a large workspace, and a high acceleration capability. They have optimized their device in terms of workspace and dexterity.

The present work introduces a new concept for an SPM which allows for significant higher mechanical rigidity and lower inertia. This is realized by a mechanically overdetermined design through a central hollow shaft that supports translational and gravitational forces. As a result, high mechanical stiffness can be achieved with regards to translational DoF. At the same time the moving links can be designed to be lighter as they are not responsible for translational stiffness.

Moreover, for the first time in the optimization of an SPM, inertia and structural stiffness are considered in addition to workspace and dexterity. Figure 1 shows the CAD model and the functional demonstrator of the proposed coaxial SPM-based rotational haptic device, namely CoaxHaptics-3RRR. Preliminary findings were initially presented in a late-breaking results poster by the authors [16].

The main contributions of this work are (i) a proposal of a new concept for a mechanically overdetermined SPM-based rotational haptic device, (ii) a functional demonstrator of the device with optimized workspace, manipulability, inertia, and structural stiffness, and (iii) an experimental validation of the proposed features.

The rest of the paper is composed as follows: Section II analyzes the proposed mechanism's kinematics, dynamics, and stiffness; Section III describes a multiobjective optimization of the proposed mechanism design; Section IV presents the functional demonstrator of the designed CoaxHaptics-3RRR; Section V experimentally validates the proposed design; Section VI concludes the paper with discussions on future works.

II. Analysis of the Proposed Mechanism

The newly introduced CoaxHaptics-3RRR is shown in Fig. 1. Compared to existing SPMs, it incorporates a central hollow shaft connected to the moving platform via a spherical bearing. This design contributes to high structural rigidity without increasing moving mass. On the other hand, the hollow shaft makes the mechanism mechanically overdetermined. However, this over-determination does not cause issues such as high tension in the mechanical parts or increased friction. Furthermore, tension during assembly is minimized by fixing the hollow shaft and the spherical bearing only in the final stage of assembly.

This section describes the modeling phase of the SPM, which includes kinematics, dynamics, and stiffness analysis. Note that the central hollow shaft of the CoaxHaptics-3RRR does not impact the analysis presented in this section. Therefore, existing methodologies for kinematics, dynamics, and stiffness, particularly those from [17], [18], [19], can be employed and adapted. This paper provides a condensed version of the methodology, emphasizing aspects that are of particular importance for haptic interaction applications, such as the minimization of inertia and maximization of rotational stiffness.

A. Kinematic Model

This subsection summarizes the kinematic model analysis of SPMs that is presented in detail in [17]. The inverse and forward kinematics are given, and the Jacobian matrix

is obtained. It is well-known that for parallel kinematic structures, the solution of forward kinematics is generally not straightforward while the inverse kinematics becomes trivial.

The manipulator consists of proximal and distal limbs and an end-effector, which in SPMs is commonly referred to as mobile platform. The kinematic model of a single kinematic chain (i.e. a leg) of our SPM is shown in Fig. 2. The base frame and the mobile platform frame locations are symbolized as O_b and O_m, respectively. O_m is also the location of the rotation center of the manipulator. All active and passive (non-actuated) joint axes are intersecting in that point.

The angles of the actuated joints are q_{11}, q_{21}, and q_{31}. The parameters α_1, α_2 and r are the same for the three legs (see Fig. 2), where the angles α_1 and α_2 define proximal and distal links, respectively, and the radius r stands for the distance between each joint to the center of rotation O_m. The unit vector

$$\vec{p}_{i1} = \begin{bmatrix} 0 & 0 & -1 \end{bmatrix}^T \tag{1}$$

points from O_m towards the active joint q_{i1} with $i \in \{1,2,3\}$. Similarly, the vectors $\vec{p}_{i2}$ and $\vec{p}_{i3}$ point towards the end of the proximal and distal links respectively.

The vector $\vec{p}_{i2}$ is found by rotating $\vec{p}_{i1}$ with

$$\vec{p}_{i2} = \mathbf{R_z}(q_{i1})\mathbf{R_x}(\alpha_1)\vec{p}_{i1}\,, \tag{2}$$

where $\mathbf{R_x}$ and $\mathbf{R_z}$ are rotation matrices for rotation around x and z axes, respectively. To find the forward kinematics, the geometric relations

$$\vec{p}_{i2}\vec{p}_{i3} = \cos\alpha_2 \tag{3}$$

$$\vec{p}_{i3}\vec{p}_{j3} = \cos\alpha_3, \quad i,j = 1,2,3 \quad i \neq j \tag{4}$$

$$\left\|\vec{p}_{i3}\right\| = 1 \tag{5}$$

are solved together numerically in Matlab, where $\|.\|$ stands for the Euclidean norm of a vector and $\alpha_3 = 2\sin^{-1}\left(\sin\beta\cos\frac{\pi}{6}\right)$ for the angle between the vectors of $\vec{p}_{i3}$ that are directed from center of rotation (O_m) to the end of distal links (see Fig. 2). To obtain a symmetric design of the mobile platform, α_3 is the same between each pair of the three vectors $\vec{p}_{i3}$. The solution of the forward kinematics results by determining all the vectors $\vec{p}_{i3}$.

Inverse kinematics is the solution of joint variables for giving end-effector pose. As it was pointed out before, inverse kinematics is rather straightforward. Substitution of the vectors $\vec{p}_{i2}$ and $\vec{p}_{i3}$ into (3) yields the quadratic equation

$$a_i x_i^2 + 2b_i x_i + c_i = 0. \tag{6}$$

As stated in [17]

$$\begin{aligned} a_i &= -\vec{p}_{i3y} - \vec{p}_{i3z}\cos\alpha_1 - \cos\alpha_2 \\ b_i &= -\vec{p}_{i3x}\sin\alpha_1 \\ c_i &= -\vec{p}_{i3y}\sin\alpha_1 - -\vec{p}_{i3z}\cos\alpha_1 - \cos\alpha_2 \end{aligned} \tag{7}$$

with

$$x_i = \tan\left(\frac{q_{i1}}{2}\right). \tag{8}$$

After a series of mathematical manipulations, active joint angles q_{i1} become

$$q_{i1} = 2\tan^{-1}\left[\frac{-b_i \pm \sqrt{\Delta_i}}{2a_i}\right], \tag{9}$$

where $\Delta_i = \sqrt{b_i^2 - 4a_i c_i}$. To obtain the Jacobian matrix, the time derivative of (3) is taken, yielding

$$\dot{\vec{p}}_{i2}\vec{p}_{i3} + \vec{p}_{i2}\dot{\vec{p}}_{i3} = 0. \tag{10}$$

The relation between angular and linear velocities is defined by the Jacobian matrix

$$\mathbf{J}\dot{\vec{q}}_1 = (\mathbf{\Gamma^{-1}\Lambda})\dot{\vec{q}}_1 = \vec{\omega}, \tag{11}$$

where $\vec{q}_1 = (q_{11}, q_{21}, q_{31})^T$ is the vector of the actuated joint angles, $\vec{\omega}$ is the end-effector angular velocity vector, $\mathbf{\Gamma}$ and $\mathbf{\Lambda}$ are 3×3 matrices, which are given by

$$\mathbf{\Gamma} = \begin{bmatrix} (\vec{p}_{31}\times\vec{p}_{21})^T \\ (\vec{p}_{32}\times\vec{p}_{22})^T \\ (\vec{p}_{33}\times\vec{p}_{23})^T \end{bmatrix} \tag{12}$$

$$\mathbf{\Lambda} = \begin{bmatrix} (\vec{p}_{11}\times\vec{p}_{21})^T\vec{p}_{31} & 0 & 0 \\ 0 & (\vec{p}_{12}\times\vec{p}_{22})^T\vec{p}_{32} & 0 \\ 0 & 0 & (\vec{p}_{13}\times\vec{p}_{23})^T\vec{p}_{33} \end{bmatrix}. \tag{13}$$

B. Inertia Minimization in the Sense of Energies

In this paper, dynamic analysis of the manipulator is accomplished based only on the kinetic energy of the manipulator following Lagrange method, since the kinetic energy provides information about the inertia of the system. In Fig. 3, the center of mass of the proximal and distal links are described. The kinetic energy becomes

$$E = \frac{1}{2}m_1\dot{\vec{p}}_{gi1}^T\dot{\vec{p}}_{gi1} + \frac{1}{2}\dot{q}_{i1}^T\mathbf{I_1}\dot{q}_{i1} + \frac{1}{2}m_2\dot{\vec{p}}_{gi2}^T\dot{\vec{p}}_{gi2} + \frac{1}{2}\vec{\omega}^T\mathbf{I_2}\vec{\omega}, \tag{14}$$

where m_1 and m_2 are the masses, $\vec{p}_{g1i}$ and $\vec{p}_{g2i}$ are center of mass velocities, $\mathbf{I_1}$ and $\mathbf{I_2}$ are the moment of inertia of the proximal and distal links, respectively.

C. Stiffness Model

This subsection follows the procedure for the stiffness matrix calculation described in [19] and adapts it to our system. There are various methods to obtain the stiffness model of a manipulator, which are structural matrix, finite element, and virtual joint methods [20]. The virtual joint method is preferred in this study due to its computational efficiency and ease of describing the model. The virtual joint variables are the variables that define the spatial deflection or displacement of the links. Stiffness analysis provides information on the deflection of the mechanism under the effect of force or torque. For haptic devices, high structural stiffness is necessary to achieve proper haptic sensation. Figure 4 shows the kinematic topology of the mechanism.

The transformation matrix for a single link is

$$\mathbf{H_{Ki}} = \mathbf{H_{Ki1}}\mathbf{H_{Ki2}}\mathbf{H_{Ki3}}, \tag{15}$$

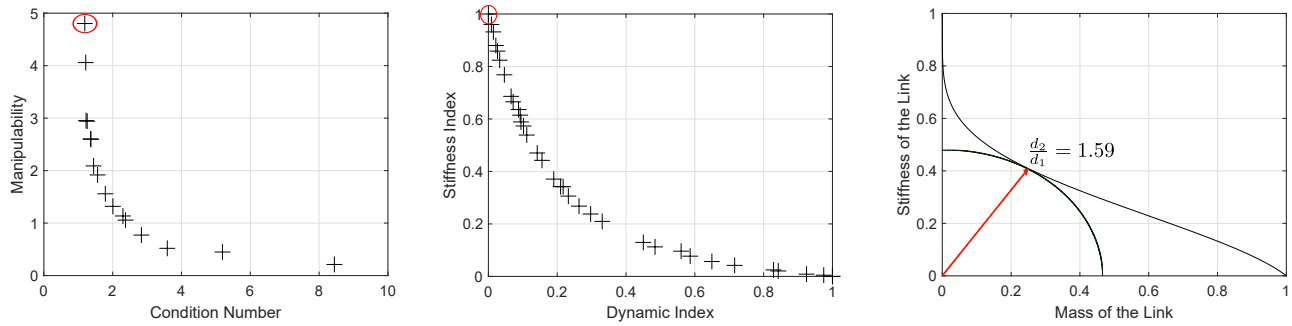

(a) condition number over manipulability (b) normalized stiffness index over normalized dynamic index (c) cross-section related optimization

Fig. 5: Pareto-front solutions for the four objective functions (in (a) and (b)) and the cross-section (in (c)).

where $\mathbf{H_{Ki}}$ is the homogeneous transformation matrix that consists of active, passive, and virtual joint variables. The homogeneous transformation matrices from base to the end of proximal link, from the end of proximal link to the end of distal link, and from the end of distal link to end of mobile platform is represented by $\mathbf{H_{ki1}}$, $\mathbf{H_{ki2}}$, and $\mathbf{H_{ki3}}$, respectively.

To obtain an extended Jacobian matrix, which consist of active, passive, and virtual joint variables, angular and linear velocity coefficients should be acquired. The derivative of the above transformation matrix with respect to joint variables yields,

$$\frac{\partial \mathbf{H_{Ki}}}{\partial \vec{q}_{ik}} = \begin{bmatrix} \frac{\partial \mathbf{R_{Ki}}}{\partial \vec{q}_{ik}} & \frac{\partial \vec{r}_{Ki}}{\partial \vec{q}_{ik}} \\ [0]^T_{1x3} & 1 \end{bmatrix}, \tag{16}$$

where $\vec{q}_{ik}$ includes active, passive, and virtual joint variables [20], $\mathbf{R_{Ki}}$ and $\vec{r}_{Ki}$ denote the orientation matrix and position vector of the mobile platform, respectively. Hence, angular and linear velocity coefficients become

$$\boldsymbol{\lambda_{ik}} = \frac{\partial \mathbf{R_{Ki}}}{\partial \vec{q}_{ik}} \mathbf{R^T_{Ki}} \tag{17}$$

and

$$\vec{\Upsilon}_{ik} = \frac{\partial \vec{r}_{ki}}{\partial \vec{q}_{ik}}. \tag{18}$$

Here, $\boldsymbol{\lambda_{ik}}$ is a skew-symmetric matrix that consists of angular velocity coefficient terms. To convert skew-symmetric matrix to a vector, we utilize so called '*vec*' operator as

$$\vec{\lambda}_{ik} = vec\left(\boldsymbol{\lambda_{ik}}\right). \tag{19}$$

Thus, the extended Jacobian matrix becomes

$$\mathbf{J_{Ki}} = \begin{bmatrix} \vec{\lambda}_{ik} \\ \vec{\Upsilon}_{ik} \end{bmatrix}_{6\times 1}. \tag{20}$$

Herein, $\mathbf{J_{Ki}}$ composes of active, passive, and virtual joint properties, which can be represented as $\mathbf{J_{Ai}}$, $\mathbf{J_{Pi}}$, and $\mathbf{J_{\theta i}}$, respectively. The whole deflection which occurred at the mobile platform is

$$\Delta\vec{X} = \mathbf{J_{Ai}}\Delta\vec{q}_{i1} + \mathbf{J_{Pi}}[\Delta\vec{q}_{i2}\ \Delta\vec{q}_{i3}]^T + \mathbf{J}_{\boldsymbol{\theta}_i}\Delta\vec{\theta}_i, \tag{21}$$

where $\Delta\vec{q}_{i1}$, $\Delta\vec{q}_i$, and $\Delta\vec{\theta}_i$ are the displacements that occurred in active, passive, and virtual joints, respectively [19]. The corresponding torque value, which is formed due to the external wrench $\vec{W}_{\text{ext}} = [\vec{F}^T\ \vec{M}^T]^T$, is

$$\vec{\tau}_i = \mathbf{J^T_{Ki}}\vec{W}_{\text{ext}}. \tag{22}$$

The deviation $\Delta\vec{\theta}_i$ is defined by the joint space stiffness matrix $\mathbf{K}_{\theta_i}$ with

$$\vec{\tau}_i = \mathbf{K}_{\boldsymbol{\theta}_i}\Delta\vec{\theta}_i. \tag{23}$$

As passive joints do not generate reaction torque about their rotation axis,

$$\mathbf{J^T_{Pi}}\vec{W}_{\text{ext}} = 0. \tag{24}$$

The kinetostatic model of the mechanism is procured by combinations of (21), (22), and (24) as

$$\begin{bmatrix} \mathbf{J}_{\theta_i}\mathbf{K^{-1}_{\theta_i}}\mathbf{J^T_{\theta_i}} & \mathbf{J_{Pi}} \\ \mathbf{J^T_{Pi}} & \mathbf{[0]}_{2x2} \end{bmatrix} \begin{bmatrix} \vec{W}_{\text{ext}} \\ \Delta\vec{q}_i \end{bmatrix} = \begin{bmatrix} \Delta\vec{X} \\ \mathbf{[0]}_{2x1} \end{bmatrix}. \tag{25}$$

Finally, the construction of the Cartesian stiffness matrix is completed by inverting the left-hand side of the equation

$$\begin{bmatrix} \mathbf{J}_{\theta_i}\mathbf{K^{-1}_{\theta_i}}\mathbf{J^T_{\theta_i}} & \mathbf{J_{Pi}} \\ \mathbf{J^T_{Pi}} & \mathbf{[0]}_{2x2} \end{bmatrix}^{-1} = \begin{bmatrix} \mathbf{K_{Ci}} & \sim \\ \sim & \sim \end{bmatrix}, \tag{26}$$

where $\mathbf{K_{Ci}}$ is the Cartesian stiffness matrix that belongs to ith leg. To find the total Cartesian matrix of the mechanism, the Cartesian stiffness matrices of each leg are accumulated,

$$\mathbf{K_c} = \sum_{i=1}^{3} \mathbf{K_{ci}}. \tag{27}$$

III. Multi-Objective Optimization

Haptic device optimization is usually composed of different objective functions [21]. To get precise results from the optimization task, the problem should be stated as a multi-objective optimization problem. There are several commonly used algorithms that are used in the development of haptic devices [22]. The non-linear behavior of the parallel mechanisms and non-convex features of the performance indices make the optimization task arduous. Therefore, to overcome this difficulty, several evolutionary algorithms were developed. In this paper, we use a genetic algorithm as used by [23], [24] because of its good performance

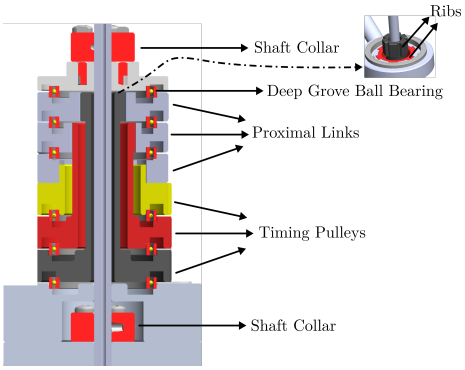

Fig. 6: Sectional view of the coaxial transmission mechanism (CTM).

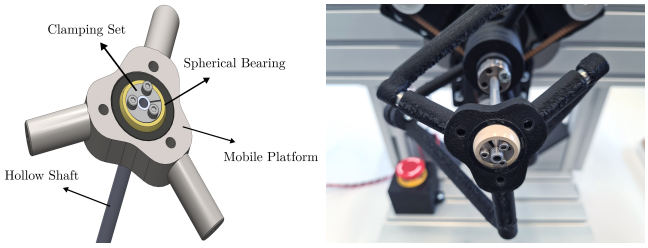

(a) CAD (b) photo

Fig. 7: Design of the mobile platform with its components. i.e. hollow shaft, spherical bearing, clamping set.

and convenience for implementation. In comparison to [23], [24], besides kinematics and dynamics, we also include the structural stiffness of the device as an objective function, because this is an important property for haptic devices that need to be capable of rendering large impedance ranges [25]. This section describes the multi-objective optimization that was carried out by using a genetic algorithm.

TABLE I: Design variables and bounds.

Design Variables	α_1°	α_2°	β°	$d_2(m)$	$r(m)$
Upper Bound	135°	135°	135°	0.030	0.3
Lower Bound	25°	25°	25°	0.005	0.1

A. Definition of Objective Functions

In this part, the objective functions related to the kinematics (manipulability and condition number), dynamics, stiffness are described. The design variables and bounds are given in Table I. The optimization is divided into two consecutive optimization steps. The design variables related to the dynamics and stiffness do not affect the manipulability and condition number. Hence, first, an optimization procedure is accomplished by considering manipulability and condition number [26], [27]. Thereafter, an optimization considering dynamics and stiffness is conducted. In the following, four objective functions are determined.

The condition number of the SPM is given by

$$\kappa(\mathbf{J}) = \|\mathbf{J}\|\|\mathbf{J^{-1}}\| = \frac{min(eig(\mathbf{J}))}{max(eig(\mathbf{J}))}, \tag{28}$$

where *eig* is the eigenvalues of the matrix. While the physical meaning of manipulability describes an operator's ease of moving the mechanism at a position, the condition number describes the proximity of the manipulator's pose to a singularity. The Euclidean norm is used to calculate κ in (28). The global conditioning index (GCI) [28] can now be identified over the workspace as

$$f_1 : GCI = \frac{1}{n}\sum_{k=1}^{n}\frac{1}{\kappa(\mathbf{J})} \tag{29}$$

where n is the number of workspace points that are chosen by the stochastic approach. The manipulability η is an index that helps to represent the optimum pose of the manipulator,

$$f_2 : \eta = \sqrt{det(\mathbf{J}\mathbf{J}^\mathbf{T})}. \tag{30}$$

The objective functions related with the dynamics is

$$f_3 : E, \tag{31}$$

for given joint velocities as in (14). The main idea here is to reduce the energy E of the SPM, which leads to a minimization of the link masses. In this work, for simplicity only the rotation around the axis of the central shaft in zero configuration ($q_{11} = q_{21} = q_{31} = 0^\circ$) was considered for (31). Hence, for the optimization it was assumed that all three active joints q_{i1} rotated with the same velocity, i.e.

$$\dot{q}_{11} = \dot{q}_{21} = \dot{q}_{31}. \tag{32}$$

The objective function associated with structural stiffness is

$$f_4 : \frac{1}{det(\mathbf{K_c})}. \tag{33}$$

Minimizing the objective function f_4 leads to an increase in structural stiffness, $\mathbf{K_c}$.

Based on the four defined objective functions, the multi-objective optimization problem is formulated as

$$\begin{cases} \text{minimize} & f_1, f_2, f_3, f_4 \\ \text{over} & x = [\alpha_1, \alpha_2, \beta, d_2, r] \\ \text{constraints} & det(\mathbf{J}) \neq 0 \end{cases} \tag{34}$$

TABLE II: Parameters for genetic algorithm.

Population	Reproduction	Mutation	Crossover	Selection
200	0.8	constraint dependent	1	2

B. Pareto-Front Solutions

The multi-objective optimization task was carried out by using a genetic algorithm based on NSGA-II [29], of which parameters represented in Table II. The condition number and manipulability solutions are selected considering the point at which the condition number is close to 1 and the manipulability is highest, as shown by the red circle in Fig. 5a. The selection of the optimal solution (Fig. 5b) for dynamics and stiffness of the mechanism is done by considering the solution that has highest natural frequency, i.e. highest stiffness and lowest inertia. Note that the values for the stiffness and dynamic indices are normalized to values between 0 and 1 for comparison purposes. The selected

TABLE III: Obtained design parameters.

Design Variables	α_1°	α_1°	β°	$d_2(m)$	$r(m)$
Obtained Parameters	47.25°	80°	75°	0.01	0.120

TABLE IV: System specifications of CoaxHaptics-3RRR

Properties	System Specifications
DoF	3 active (rotational DoF)
Number of Joints	3 active, 6 passive joints
Mass	approx. 1500 g
Size	100 × 100 × 210 mm (length × width × height)
Workspace	unlimited × ±55° × ±55° (roll × pitch × yaw)
Motors	3 × Maxon EC flat brushless DC motor with encoder
Controller	3 × Elmo Motion Control Gold Whistle

solutions are illustrated in Fig. 5a and Fig. 5b. The obtained design parameters are presented in Table III.

The studies [23], [24] also found similar results to ours except for the angles α_1 and β, which were obtained smaller than found in mentioned studies. We observed in our work, which considers the structural stiffness of the SPM as an objective function in addition to the kinematic and dynamic objective functions, that smaller α_1 and β angles result in higher structural stiffness of the SPM.

The cross-sections of the links are optimized by evaluating the stiffness and mass performance indices for a single link, assuming the links are tubular cylinders (refer to [19] for the stiffness calculation of tubular links). The optimum cross-section ratio is determined by finding the point on the curve in Fig. 5c closest to the origin. For our 3D-printed parts made of polylactic acid (PLA), the optimum ratio between outer d_2 and inner diameter d_1 of the link is found as 1.59 assuming equal weighting of link stiffness and mass (see Fig. 5c). In above optimization of stiffness and dynamic indices, only d_2 is optimized, and the corresponding d_1 results from this ratio.

IV. Functional Demonstrator

After obtaining the optimum design parameters in terms of kinematics, dynamics and stiffness, the functional demonstrator was constructed. Ball bearings are used in the design of coaxial transmission mechanism (CTM). Figure 6 shows the sectional view of the CTM architecture.

A hollow shaft was integrated in the center of the manipulator to support lateral and vertical forces acting on the mobile platform [30]. In addition, the hollow shaft can carry cables to allow additional user interfaces, such as push buttons on the rotary knob, to be connected. The timing pulleys are shown in yellow, red, and black color and are connected to the corresponding proximal links, respectively. For this purpose, the timing pulleys top side is provided with a ribbed structure. These timing pulleys are driven by motors via timing belts as shown in Fig. 1a. The entire manipulator is assembled on a carrier plate together with the motor housings. Upward and downward shaft collars serve to hold the CTL in place under gravity and other forces acting in the direction of the hollow shaft.

TABLE V: Results for mechanical stiffness experiments.

Direction	Applied Force (N)	Corresponding Torque (Nmm)	Measured Deflection (rad)	Calculated Stiffness (Nmm/rad)
lateral	3	90	0.04	2250
	6	180	0.09	1805
vertical	5	150	0.0798	1888
	10	300	0.1194	2512
	15	450	0.1974	2280

At the top of the hollow shaft, the mobile platform is assembled with a spherical bearing and a clamping set. The design of the mobile platform is presented in Fig. 7. The main idea behind the design of the knob is that the mobile platform should be grasped as close as possible to the center of rotation of the haptic device. This allows the user to turn the manipulator with the greatest ease because user interacts with the manipulator closer to its center of rotation point.

Several parts including the links, timing pulleys, and the knob are manufactured with additive manufacturing technology using Fused Deposition Modelling (FDM) technique. The system specifications of CoaxHaptics-3RRR are presented in Table IV.

V. Test and Evaluation

Several tests have been conducted to show the performance of the proposed mechanism. First, the rotational structural stiffness was determined around two axes. Second, the user could freely move the mobile platform and thus explore the workspace. Third, the impedance range of the proposed mechanism has been experimentally revealed. Lastly, the inertia matrices were calculated for different configurations and thus the coupling between different DoF was determined.

For the first test, the timing belt pulleys of the proposed manipulator were mechanically locked to measure the corresponding structural stiffness values while the manipulator is in the configuration shown in Fig. 1b. To fix the structure two clamps were used. A spring balance was used to apply different forces to the mobile platform in two directions (vertical and lateral).

Firstly, lateral forces were applied to the haptic device. The force values were measured by the spring balance and the corresponding deflection of the end-effector was determined with the help of a laser pointer. Secondly, the same experiment was conducted in the vertical direction.

The results are presented in Table V. The structural stiffness in the two directions turned out to be similar at around 2000 Nmm/rad. The structural stiffness of the mechanism in the translational directions is mainly determined by the central hollow shaft. It can be easily calculated from the material properties and dimensions.

In the first phase, it was found that the mechanism's workspace covers a wide portion of the hands workspace, which are 100° for the roll and pitch. In particular, when the human arm was positioned so that its axis was aligned with the axis of the central hollow shaft, the limit of the working range was rarely reached. Therefore, our device

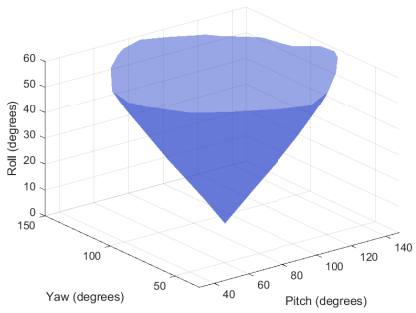

Fig. 8: Workspace of the CoaxHaptics-3RRR.

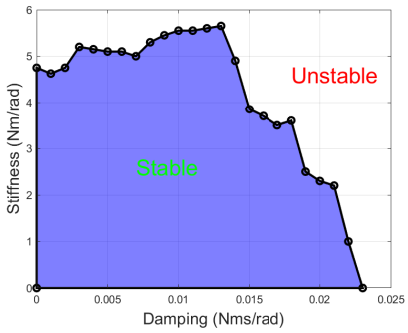

Fig. 9: Stable impedance range of the CoaxHaptics-3RRR.

covers a larger workspace compared to the SHaDe [15], which has a workspace of $\pm 90^\circ \times \pm 45^\circ \times \pm 45^\circ$ (roll $\times$ pitch $\times$ yaw). Furthermore, our device can perform rotational motions while maintaining a constant orientation of its mobile platform, providing significant benefits for various applications.

This was mainly due to the unlimited rotatability around the axis of the hollow shaft, as humans have the largest rotation range in this DoF [31]. The workspace of the CoaxHaptics-3RRR is represented in Fig. 8. The workspace of CoaxHaptics-3RRR is a conic shape that is found by using forward kinematics. It has further been found that the mechanical over-determination does not lead to any perceivable tension or increased friction over the workspace.

To reveal the stable range of impedances that the device can render, experiments have been conducted. A virtual wall was generated around the end effector of the device and a couple of weights were hanged to the mobile platform to interact with the virtual environment. The impedance range of the device is illustrated in Fig. 9. While the maximum renderable stiffness value without virtual damping is 4.75 Nm/rad, it can be increased up to 5.65 Nm/rad. Unfortunately, studies on the development of kinesthetic haptic devices typically do not investigate the stable impedance range that can be stably rendered. Consequently, to the best of our knowledge, there is no published impedance range for an orientational haptic device that we can compare with our device.

To investigate the inherent coupling of the device, the dynamic analysis of the mechanism is performed and mass matrix is obtained, by utilizing the source code provided by [12], for different configurations of the device. For the home configuration, when all joint variables are set to zero, the mass matrix shows almost diagonal form and the values of the diagonal terms are closed to each other, meaning that inertia of the rotational DoF is uniformly distributed as illustrated in the first image on the left of Fig. 10. When we tilt the device from the home configuration by 20° and 30°, the coupling terms in the mass matrix increase, as shown in Fig. 10 (second and third columns). However, the inertia matrix remains uniform, with diagonal terms larger than the off-diagonal terms. The coupling terms become more significant at a 45° tilt (the last column), where the device nearly reaches its workspace boundary.

The uniform and diagonal structure of the inertia matrix aids in controlling the device. It maintains these properties across a large portion of its workspace, which benefits optimal performance in haptics and telerobotic applications.

VI. Conclusion

This paper presents CoaxHaptics-3RRR, a novel coaxial spherical haptic interaction device. In comparison to other similar mechanisms, the device is equipped with a central hollow shaft that makes it stiff with regard to the translational directions and thus allows for lighter links. A multi-criteria optimization method was used to find a set of design parameters that yield an optimal design in terms of kinematics, dynamics, and stiffness.

Based on these design parameters, a functional demonstrator was built and preliminary tests were carried out. The functional demonstrator contains a new interconnectable CTM to operate the links from the motors. Its knob allows the user to grasp the device near the center of rotation, thus avoiding the negative effects of offsets on effective inertia at the user hand.

The conducted tests validate the approach of the mechanism. The mechanism's mechanical overdetermination does not restrict the workspace, nor does it lead to tension or increased friction. With these tests also the rotational stiffness in lateral and vertical direction was determined. It was further experienced that the designated manipulator covers a large proportion of human wrist. In particular the unlimited rotation around the axis of the hollow shaft appears beneficial if aligned to the axis of the forearm, in which the human has highest angular range. Furthermore, the stable range of impedance demonstrates that CoaxHaptics-3RRR can provide a wide range of rotational damping and stiffness. This versatility enables the device to be used in a vast variety of applications.

The performed dynamics analysis shows that the device preserves diagonal shape of its inertia matrix within large proportion of the workspace. As a future work, we will investigate the extension to a full 6-DoF mechanism for example by attaching the device to a collaborative robot. Furthermore, we aim to investigate the performance of the proposed device in multi-DoF haptic and telerobotic applications, and conduct comparisons with other torque feedback haptic devices.

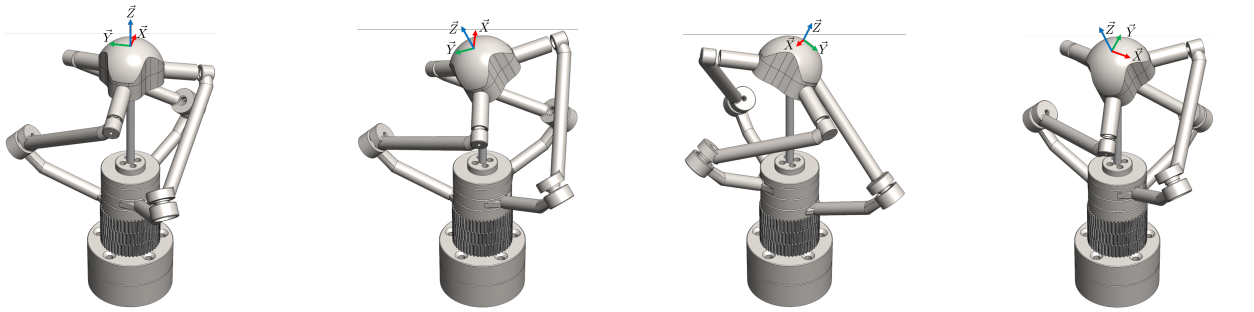

$$\begin{bmatrix} 0.0764 & -0.0030 & -0.0036 \\ -0.0030 & 0.0501 & -0.0001 \\ -0.0036 & -0.0001 & 0.0584 \end{bmatrix} \quad \begin{bmatrix} 0.0763 & 0.0214 & 0.0140 \\ 0.0214 & 0.1011 & 0.0173 \\ 0.0140 & 0.0173 & 0.0505 \end{bmatrix} \quad \begin{bmatrix} 0.0767 & 0.0279 & 0.0256 \\ 0.0279 & 0.1507 & 0.0611 \\ 0.0256 & 0.0611 & 0.0728 \end{bmatrix} \quad \begin{bmatrix} 0.0769 & 0.0959 & 0.0755 \\ 0.0959 & 0.8227 & 0.4884 \\ 0.0755 & 0.4884 & 0.3412 \end{bmatrix}$$

Fig. 10: Inertia matrix ($10^{-3} kg\, m^2$) for different configurations.

REFERENCES

[1] cyberneticzoo.com, "1948 – GE Master-Slave Manipulator – John Payne," 2014, "http://cyberneticzoo.com/teleoperators/1948-ge-master-slave-manipulator-john-payne-american/" (date last accessed: May 27, 2024).

[2] T. H. Massie and J. K. Salisbury, "The PHANToM haptic interface: A device for probing virtual objects," in *ASME Winter Annual Meeting, Symposium on Haptic Interfaces for Virtual Environment and Teleoperator Systems*, Chicago, 1994, pp. 295–302.

[3] "Omega.3 parallel haptic device," date last accessed: May 27, 2024. [Online]. Available: http://forcedimension.com/images/doc/specsheet_-_omega3.pdf

[4] S. Martin and N. Hillier, "Characterisation of the novint falcon haptic device for application as a robot manipulator," in *Australasian Conf. on Robotics and Automation (ACRA)*. Citeseer, 2009, pp. 291–292.

[5] M. Vulliez, S. Zeghloul, and O. Khatib, "Design strategy and issues of the delthaptic, a new 6-dof parallel haptic device," *Mechanism and Machine Theory*, vol. 128, pp. 395–411, 2018.

[6] M. Kühne, J. Potzy, R. García-Rochín, P. van der Smagt, and A. Peer, "Design and evaluation of a haptic interface with octopod kinematics," *IEEE/ASME Trans. on Mechatronics*, vol. 22, no. 5, pp. 2091–2101, 2017.

[7] A. M. Tahmasebi, B. Taati, F. Mobasser, and K. Hashtrudi-Zaad, "Dynamic parameter identification and analysis of a phantom haptic device," in *IEEE Int. Conf. on Control Applications*. IEEE, 2005, pp. 1251–1256.

[8] A. Tobergte, P. Helmer, U. Hagn, P. Rouiller, S. Thielmann, S. Grange, A. Albu-Schäffer, F. Conti, and G. Hirzinger, "The sigma.7 haptic interface for MiroSurge: A new bi-manual surgical console," in *IEEE/RSJ Int. Conf. on Intelligent Robots and Systems (IROS)*. IEEE, 2011, pp. 3023–3030.

[9] P. A. Millman and J. E. Colgate, "Design of a four degree-of-freedom force-reflecting manipulandum with a specified force/torque workspace," in *IEEE Int. Conf. on Robotics and Automation (ICRA)*. IEEE Computer Society, 1991, pp. 1488–1489.

[10] M. Z. Huang, S.-H. Ling, and Y. Sheng, "A study of velocity kinematics for hybrid manipulators with parallel-series configurations," in *IEEE Int. Conf. on Robotics and Automation (ICRA)*. IEEE, 1993, pp. 456–461.

[11] H. Qin, A. Song, Y. Liu, G. Jiang, and B. Zhou, "Design and calibration of a new 6 dof haptic device," *Sensors*, vol. 15, no. 12, pp. 31 293–31 313, 2015.

[12] A. Hassani, A. Bataleblu, S. Khalilpour, H. D. Taghirad, and P. Cardou, "Dynamic models of spherical parallel robots for model-based control schemes," *arXiv preprint arXiv:2110.00491*, 2021.

[13] H. Asada and J. Granito, "Kinematic and static characterization of wrist joints and their optimal design," in *IEEE Int. Conf. on Robotics and Automation (ICRA)*, vol. 2. IEEE, 1985, pp. 244–250.

[14] C. M. Gosselin and É. St-Pierre, "Development and experimentation of a fast 3-dof camera-orienting device," *The Int. Journal of Robotics Research*, vol. 16, no. 5, pp. 619–630, 1997.

[15] L. Birglen, C. Gosselin, N. Pouliot, B. Monsarrat, and T. Laliberté, "SHaDe, a new 3-dof haptic device," *IEEE Trans. on Robotics and Automation*, vol. 18, no. 2, pp. 166–175, 2002.

[16] H. T. Dinc, T. Hulin, M. Rothammer, H. Song, B. Willberg, B. Pleintinger, J.-H. Ryu, and C. Ott, "CoaxHaptics-3RRR: A novel coaxial spherical parallel haptic device (late breaking results poster)," in *IEEE/RSJ Int. Conf. on Intelligent Robots and Systems (IROS)*, Oct. 2022. [Online]. Available: https://elib.dlr.de/189356/

[17] I. Tursynbek, A. Niyetkaliye, and A. Shintemirov, "Computation of unique kinematic solutions of a spherical parallel manipulator with coaxial input shafts," in *IEEE Int. Conf. on Automation Science and Engineering (CASE)*. IEEE, 2019, pp. 1524–1531.

[18] F. C. Park, B. Kim, C. Jang, and J. Hong, "Geometric algorithms for robot dynamics: A tutorial review," *Applied Mechanics Reviews*, vol. 70, no. 1, 2018.

[19] İ. Görgülü, G. Carbone, and M. İ. C. Dede, "Time efficient stiffness model computation for a parallel haptic mechanism via the virtual joint method," *Mechanism and Machine Theory*, vol. 143, p. 103614, 2020.

[20] A. Pashkevich, D. Chablat, and P. Wenger, "Stiffness analysis of overconstrained parallel manipulators," *Mechanism and Machine Theory*, vol. 44, no. 5, pp. 966–982, 2009.

[21] S. Khan, A. Ahmad, and K. Andersson, "Design optimization of the tau haptic device," in *Int. Congress on Ultra Modern Telecommunications and Control Systems and Workshops (ICUMT)*, 2011, pp. 1–8.

[22] X. Sun, K. Andersson, and U. Sellgren, "Design optimization of haptic device - a systematic literature review," 2017, (date last accessed: May 27, 2024). [Online]. Available: http://kth.diva-portal.org/smash/record.jsf?pid=diva2%3A1155505

[23] G. Wu, "Multiobjective optimum design of a 3-rrr spherical parallel manipulator with kinematic and dynamic dexterities," *Modelling, Identification and Control*, vol. 33, no. 3, pp. 111–122, 2012.

[24] G. Wu, S. Caro, S. Bai, and J. Kepler, "Dynamic modeling and design optimization of a 3-dof spherical parallel manipulator," *Robotics and Autonomous Systems*, vol. 62, no. 10, pp. 1377–1386, 2014.

[25] T. A. Kern *et al.*, *Engineering Haptic Devices: A Beginner's Guide for Engineers*, T. Kern, Ed. Springer, 2009.

[26] T. Yoshikawa, "Manipulability of robotic mechanisms," *The Int. Journal of Robotics Research*, vol. 4, no. 2, pp. 3–9, 1985.

[27] J.-P. Merlet, "Jacobian, manipulability, condition number, and accuracy of parallel robots," *Journal of Mechanical Design*, vol. 128, no. 1, pp. 199–206, 06 2005. [Online]. Available: https://doi.org/10.1115/1.2121740

[28] C. Gosselin and J. Angeles, "A global performance index for the kinematic optimization of robotic manipulators," *Journal of Mechanical Design*, vol. 113, no. 3, pp. 220–226, 09 1991. [Online]. Available: https://doi.org/10.1115/1.2912772

[29] K. Deb, A. Pratap, S. Agarwal, and T. Meyarivan, "A fast and elitist multiobjective genetic algorithm: NSGA-II," *IEEE Trans. on Evolutionary Computation*, vol. 6, no. 2, pp. 182–197, 2002.

[30] T. Hulin and B. Pleintinger, "Manipulator," Patent DE 10 2019 124 358, Sep. 2019.

[31] J. M. Christensen, J. W. McBarron, J. T. McConville, W. R. Pogue, R. C. Williges, and W. E. Woodson, *Man-systems integration standards NASA-STD-3000*. National Aeronautics and Space Administration (NASA), July 1995, vol. 1, revision B.